

Benchmarking Deep Learning-Based Low Dose CT Image Denoising Algorithms

Elias Eulig, Björn Ommer, Marc Kachelrieß

Abstract—Long lasting efforts have been made to reduce radiation dose and thus the potential radiation risk to the patient for computed tomography acquisitions without severe deterioration of image quality. To this end, numerous reconstruction and noise reduction algorithms have been developed, many of which are based on iterative reconstruction techniques, incorporating prior knowledge in the projection or image domain. Recently, deep learning-based methods became increasingly popular and a multitude of papers claim ever improving performance both quantitatively and qualitatively. In this work, we find that the lack of a common benchmark setup and flaws in the experimental setup of many publications hinder verifiability of those claims. We propose a benchmark setup to overcome those flaws and improve reproducibility and verifiability of experimental results in the field. In a comprehensive and fair evaluation of several deep learning-based low dose CT denoising algorithms, we find that most methods perform statistically similar and improvements over the past six years have been marginal at best.

Index Terms—Benchmarking, deep learning, denoising, computed tomography, low dose

I. INTRODUCTION

COMPUTED tomography (CT) is an important imaging modality, with numerous applications including biology, medicine, and nondestructive testing. However, the use of ionizing radiation remains a key concern and thus clinical CT scans must follow the ALARA (as low as reasonably achievable) principle [1], [2]. Therefore, reducing the dose and thus radiation risk is of utmost importance and one of the primary research areas in the field.

A straightforward approach to reduce dose is by lowering the tube current (*i.e.*, reducing the X-Ray intensity). However, this comes at the cost of deteriorated image quality due to increased image noise and thus potentially reduced diagnostic value. To alleviate this drawback, numerous algorithms have been proposed to solve the task of low-dose CT (LDCT) denoising, *i.e.*, reducing image noise in the reconstructed image (or volume).

Iterative reconstruction (IR) techniques incorporate prior knowledge in the reconstruction process and then update the

reconstructed image iteratively. The prior knowledge may model statistical properties of the noise [3], properties of the object to be reconstructed [4], or parameters of the CT system. While IR techniques can be used to reduce numerous other artifacts compared to conventional filtered back projection (FBP), they are computationally expensive, which limits their clinical applicability. On the other hand, filtering techniques to reduce noise are fast and easy to implement into various reconstruction frameworks. The filtering may either be performed in projection domain, image domain, or both, and using a wide range of algorithms [5]–[9]. Recently deep-learning based filtering, particularly in the image domain, became increasingly popular [10]–[22]. The majority of the proposed methods learn a mapping from low-dose images to high-dose images in a supervised fashion using a deep neural network (DNN). Of the numerous proposed methods, most suggestions for improvement alter the network structure, loss function, or training strategy. Publications often claim ever improving performance which is commonly demonstrated by improved image quality metrics (*e.g.*, peak signal-to-noise ratio, structural similarity) in experiments on simulated or clinical data.

In this work, we identify several flaws in the experimental setup of such methods which limit the verifiability of the claimed improvements. These include the lack of a common benchmark dataset, the use of inadequate metrics with little relation to diagnostic value, and unfair choice of hyperparameters for reference methods. Reproducibility and verifiability of scientific results, however, is paramount to scientific advancements of a field, and thus efforts towards fair benchmarking of existing and future algorithms is of utmost importance. To this end, we make the following contributions:

- We identify multiple flaws in the experimental setup of previously proposed methods which hinder the verifiability of their claimed improvements.
- We propose a benchmark setup for deep learning-based low-dose CT denoising methods, which aims to overcome those flaws and allows for a fair evaluation of existing algorithms and those yet to come.
- In a comprehensive and fair evaluation of several existing algorithms we find that there has been little progress over the past six years and many of the newer methods perform statistically similar or worse compared to older ones.

Preprint.

Elias Eulig and Marc Kachelrieß are with the German Cancer Research Center (DKFZ), Heidelberg, Germany and Heidelberg University, Germany.

Björn Ommer is with the Ludwig Maximilian University Munich, Germany.

This work was supported in part by the Helmholtz International Graduate School for Cancer Research, Heidelberg, Germany.

Correspondence to elias.eulig@dkfz.de.

II. RELATED WORK

In this section, we review existing works on deep learning-based LDCT denoising and image quality assessment of medical images.

A. Deep Learning-based LDCT Denoising

CT image reconstruction aims at solving the linear system $Rx = p$, with $p \in \mathbb{R}^M$ denoting the measurements in projection domain, $x \in \mathbb{R}^N$ being the volume to be reconstructed, and $R \in \mathbb{R}^{M \times N}$ the Radon transform. LDCT generally aims at reconstructing x using less dose, which can be *e.g.* accomplished by lowering the tube current, thus increasing the noise in p and x , or by lowering the number of measurements M , leading to sparse-view artifacts in x . Since previous studies indicate that DNN-based correction of the former can be superior, we here consider the task of LDCT denoising [23]. Based on the domain (p , x , or both) in which they operate, deep-learning based methods for LDCT image denoising can be divided into three categories: projection-domain, image-domain and dual-domain.

Projection-domain methods aim to learn a mapping $f_\theta : p' \rightarrow p$ from low-dose projections p' to high dose projections p , where f_{θ^*} is realized by a DNN, parameterized by weights θ . These weights are either optimized in a supervised setting via

$$\theta^* = \arg \min_{\theta} \mathbb{E}_{p', p \sim \mathcal{D}^{\text{train}}} \|f_\theta(p') - p\|, \quad (1)$$

with $\|\cdot\|$ being some norm [24], [25], or unsupervised, exploiting structural similarities between adjacent projections [26], [27]. The denoised projections can then be reconstructed using either of the standard reconstruction techniques [28]–[30].

Image-domain methods aim to directly learn a mapping $g_\phi : x' \rightarrow x$ from low-dose images x' (*i.e.*, images reconstructed from low-dose projections p' using FBP) to high-dose images x . Similar to Eq. (1), weights are typically optimized in a supervised setting, where the mean-squared error (MSE), or some other pixel- or feature-based loss between prediction and high-dose image x is minimized [10]–[14], [17], [19], [21], [22], [31], or g is trained together with a discriminator in an adversarial fashion [15], [18], [20]. Notable other works investigate unsupervised- or self-supervised training strategies, or leverage the intrinsic image prior of DNNs [32].

Lastly, dual-domain methods operate in both domains x and p simultaneously, by employing two separate networks f and g , respectively. Networks are trained either separately using aforementioned loss functions [33], [34] or in an end-to-end fashion using a differentiable analytical reconstruction layer [35]–[37].

In this work we focus on image-domain methods which dominate the research field. This is mainly due to the abundance of open source datasets, where paired high- and low-dose images are readily available [38], [39]. In contrast, projection data are generally proprietary and thus difficult to access [40]. The few datasets that provide them usually do so only for a (vendor-specific) subset of the data and handling of them can be cumbersome due to (hidden) preprocessing

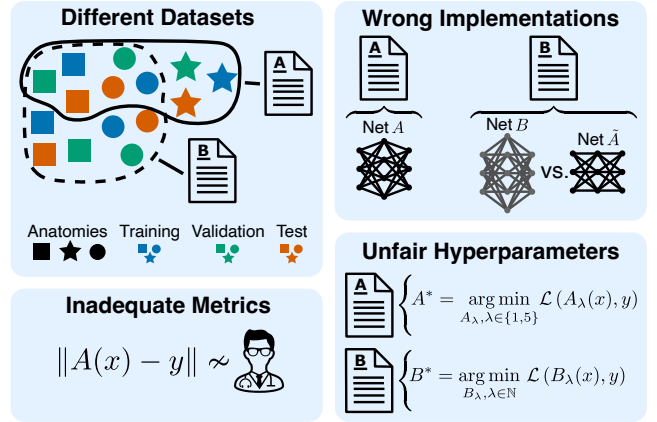


Fig. 1. Overview of flaws in the experimental setup of many deep learning-based LDCT denoising methods, that limit their verifiability.

steps in the reconstruction pipeline of the vendor [39], [41]. Many of the principles in the design of our benchmark setup, however, can be applied to the evaluation of projection-domain or dual-domain methods as well.

B. Medical Image Quality Assessment

Common full-reference quantitative measures for natural image quality assessment include the structural similarity index measure (SSIM) [42] and peak signal-to-noise ratio (PSNR). However, these metrics are usually not in agreement with human readers, which are considered the gold standard for image quality assessment of medical images [43]–[45]. These are conducted by measuring the accuracy of multiple radiologists when performing some task (*e.g.*, lesion detection or segmentation) using certain images. However, this metric relies, and is dependent, on the definition of a suitable task. Therefore, the subjective assessment of overall diagnostic quality by radiologists is a common alternative measure [46]. Nonetheless, since conducting multiple-reader studies is time-consuming and expensive, most algorithms for enhancement of medical images are still evaluated using quantitative metrics such as SSIM or PSNR.

In [45], [46], the authors find that multiple other metrics, including the visual information fidelity (VIF) [47], have higher correlation with human reader ratings compared to SSIM and PSNR for both CT and magnetic resonance (MR) images. Furthermore, notable recent works investigate the use of radiomic features to provide a clinically meaningful measure for the quality of medical images without the drawbacks of human reader studies [48]–[50].

III. FLAWS OF CURRENT EVALUATION PROTOCOLS

In this section we will outline the main problems with current evaluation protocols for deep learning-based image-domain LDCT denoising (see Fig. 1 for an overview).

A. Different datasets

Unlike in many other disciplines of computer vision, particularly image denoising of natural images [51]–[55], there

exist no consensus regarding benchmark datasets for LDCT denoising. While most methods are trained and evaluated on the dataset provided as part of the *2016 NIHAAPM-Mayo Clinic LDCT Grand Challenge* [38] or the subsequently released (significantly larger both in number of images and anatomical sites) *LDCT and Projection data* [39], authors of each method employ their own training, validation, and test split. Therefore, reported metrics across publications are not comparable. This is further exacerbated by the fact that performance of individual methods differs significantly between different anatomical sites, and images (*i.e.*, axial slices), as shown by our experiments.

B. Unfair choice of hyperparameters

Very few publications on LDCT denoising methods report the application of hyperparameter optimization [56]–[58] for their own or the considered comparison methods. In none of the respective publications of the algorithms considered in this study, exhaustive hyperparameter optimization is performed. The $3/8$ algorithms that report some form of hyperparameter optimization limit it to a grid search with few points over a single parameter (learning rate) [13], [19], a subset of the comparison methods [13], or their own method [15]. Often, authors simply use the hyperparameters reported in the reference publications [12], [13], [15]. This is particularly problematic given the choice of different datasets (*c.f.* Sec. III-A), where hyperparameters optimized by authors of method A on dataset \mathcal{D}_A may not be optimal for the dataset \mathcal{D}_B employed by authors B in their experiments.

C. Missing open source implementations

With many authors not providing open source implementations of their algorithms, researchers are often left to implement comparison methods themselves. This increases the chances of errors [59]. Additionally, changing other aspects (such as the architecture of comparison methods [13]) can further bias experimental results.

D. Inadequate metrics

Most LDCT denoising methods are evaluated using SSIM [42], PSNR, or root-mean-square error (RMSE). While these are common metrics to quantify performance for natural image denoising, they are usually not in agreement with human readers for medical images (*c.f.* Sec. II-B), making it difficult to assess the extent to which the reported improvements actually translate into clinical benefits. This could be improved by the use of quantitative measures that are more suited for medical images (*e.g.*, VIF), or experiments using human reader studies. In the respective publications of the eight algorithms considered in this study, however, most are evaluated using SSIM, RMSE, and PSNR only. Better metrics such as VIF or reader studies are employed in three publications only.

IV. BENCHMARK SETUP

In the following we present a benchmark setup to overcome the flaws of current evaluation protocols, as outlined in Sec. III that allows for a fair and clinically meaningful evaluation of DNNs for LDCT denoising.

TABLE I
HYPERPARAMETERS FOR ALL DEEP-LEARNING BASED LDCT DENOISING METHODS CONSIDERED IN THIS STUDY. THE FIRST THREE PARAMETERS ARE OPTIMIZED FOR ALL ALGORITHMS (SEPARATELY).

	Parameter	Prior
All algorithms	Learning rate	$\log \mathcal{U}(1 \times 10^{-5}, 0.01)$
	Maximum iterations	$\mathcal{U}(1 \times 10^3, 1 \times 10^5)$
	Mini-batch size	$\mathcal{U}(2, 128)$
CNN-10 (2017) [10]	Patchsize	$\mathcal{U}(32, 128)$
RED-CNN (2017) [12]	Patchsize	$\mathcal{U}(32, 128)$
WGAN-VGG (2017) [20]	β_1 of Adam	$\mathcal{U}(0.3, 0.9)$
	Loss weight: $\lambda_{\text{perceptual}}$	$\mathcal{U}(0, 1)$
	Critic updates	$\mathcal{U}(1, 5)$
	Patchsize	$\mathcal{U}(32, 128)$
ResNet (2018) [31]	Patchsize	$\mathcal{U}(32, 128)$
QAE (2019) [13]	Patchsize	$\mathcal{U}(32, 128)$
DU-GAN (2021) [15]	β_1 of Adam	$\mathcal{U}(0.3, 0.9)$
	Cutmix warmup	$\mathcal{U}(0, 1 \times 10^4)$
	Loss weight: λ_{adv}	$\mathcal{U}(0, 1)$
	Loss weight: λ_{CM}	$\mathcal{U}(0, 10)$
	Loss weight: $\lambda_{\text{px,grad}}$	$\mathcal{U}(0, 40)$
	Critic updates	$\mathcal{U}(1, 5)$
	Patchsize	$\mathcal{U}(32, 128)$
TransCT (2021) [22]	-	-
Bilateral (2022) [19]	Learning rate for σ_r	$\log \mathcal{U}(1 \times 10^{-5}, 0.01)$
	Patchsize	$\mathcal{U}(32, 128)$
	Initialization for σ_r	$\mathcal{U}(0, 1)$
	Initialization for $\sigma_{x,y}$	$\mathcal{U}(0, 1)$

\mathcal{U} : Uniform distribution; $\log \mathcal{U}$: Log-uniform distribution

A. Dataset

For our benchmark setup we utilize the *Low dose CT and Projection Dataset* [39], comprising a total of 150 scans of abdomen, head, and chest, (50 scans for each exam type) at routine dose levels. For each scan, simulated low dose-reconstructions (by means of noise insertion in the projection domain) at 25% dose for abdomen/head and 10% dose for chest, are available. For each exam type separately, data are split in 70%/20%/10% training/validation/test set and then linearly normalized to have zero mean, unit variance. During training, we employ a weighted sampling scheme such that slices from each exam type and patient are sampled with equal probability. During testing, we reduce each scan to axial regions where the brain is present (for head scans), the lung is present (for chest scans), or the lung is not present (abdomen). The code to reproduce exact dataset splits and all preprocessing is included in our benchmark suite.

B. LDCT denoising algorithms

We consider eight DNN-based LDCT denoising algorithms proposed in the literature over the past six years. In the following we briefly describe each of the methods and refer the reader to the respective publications for more details. **CNN-10 (2017) [10]** is a simple three layer CNN, trained to minimize the MSE between network output and high-dose targets. **RED-CNN (2017) [12]** and **ResNet (2018) [31]** are trained in the same fashion but employ deeper network architectures with residual connections compared to CNN-10. **WGAN-VGG (2017) [20]** and **DU-GAN (2021) [15]** are

trained in an adversarial fashion [60], [61], where DU-GAN utilizes a U-net based discriminator [62]. **QAE (2019) [13]** is based on RED-CNN in both network architecture and training scheme, but employs quadratic convolutions. **TransCT (2021) [22]** is based on transformer blocks and also trained with an MSE loss. **Bilateral (2022) [19]** uses a trainable bilateral filter instead of a DNN, and thus substantially reduces the amount of free model parameters.

C. Hyperparameter optimization

As discussed in Sec. III-B, for none of the methods a rigorous hyperparameter optimization was employed in the original publications. To ensure a fair comparison between different algorithms we optimize hyperparameters as follows. For each method we first identify hyperparameters and their suitable ranges. This includes general parameters such as learning rate, mini-batch size, patchsize and number of iterations, but also weighting factors in the loss functions (*e.g.*, to balance adversarial and pixelwise loss in a GAN setting). Suitable ranges were determined from the respective papers (with sufficient margin) and whenever two methods had the same hyperparameter (*e.g.*, learning rate or patchsize), we kept the prior distribution over the search space the same. All hyperparameters and their respective prior distributions are reported in Tab. I. For each method, we then performed a black box hyperparameter tuning using sequential-model based optimization (SMBO). Such an automatic approach is preferred over manual (human) optimization as it avoids any potential bias by the practitioner, thus ensuring fair comparison of different models. Furthermore, SMBO has been shown to outperform both human optimization and non-sequential optimization schemes like grid search or random search on a variety of DNN and dataset combinations [56], [58].

Let $t_\lambda : \{f_\theta, \mathcal{D}^{\text{train}}, \lambda\} \rightarrow \theta^*$ denote the outcome of some training run of network f on training data $\mathcal{D}^{\text{train}}$ using hyperparameters λ . The aim of hyperparameter optimization is to find an optimal set of hyperparameters $\lambda^*, i.e.,$

$$\begin{aligned} \lambda^* &= \arg \max_{\lambda} \mathbb{E}_{x, y \sim \mathcal{D}^{\text{val}}} [M(y, f_{t_\lambda}(x))] \\ &= \arg \max_{\lambda} \Psi(\lambda), \end{aligned} \quad (2)$$

where M is some metric and \mathcal{D}^{val} the validation dataset (not used during t_λ). Since evaluating $\Psi(\lambda)$ is expensive, requiring a full training run t_λ , one uses a probabilistic model p_Ψ , here constructed via Gaussian Processes, as a surrogate for Ψ . For each iteration in the optimization process, we then find the most promising next point λ , to run the costly evaluation $\Psi(\lambda)$ for, by maximizing some acquisition function. In our experiments we used the expected improvement (EI) [56] as acquisition function:

$$\text{EI}(\lambda, \Psi^*) = \int \max(z - \Psi^*, 0) p_\Psi(z|\lambda) dz, \quad (3)$$

where Ψ^* refers to the expectation of M on the validation data for the best set of hyperparameters found so far (*i.e.*, the one that maximizes the r.h.s. of Eq. (2) up to now). As metric M that is optimized by the hyperparameter optimization, we used

the SSIM for all networks. Optimizing the SSIM is favorable over other measures, since it is fast to compute, unlike *e.g.*, VIF, and not directly involved in the training process t_λ of any of the methods considered in this study (unlike *e.g.*, RMSE). Further, note that for methods using a vanilla GAN loss, *e.g.*, [15], simply minimizing the validation loss would not be suitable as it is not directly related to training progress. For each method, we perform 50 iterations of SMBO, sufficient to ensure convergence for all algorithms, as verified by our experiments.

After an optimal set of hyperparameters λ^* was found, we retrained a method using λ^* ten times with different random seeds. If not stated otherwise, all reported standard deviations and significance tests (to compare two methods) are computed over those ten training runs.

D. Metrics

We evaluate all methods on the same test set comprising a total of 15 scans (5 head/chest/abdomen) using three common full-reference measures of image quality: SSIM, PSNR¹, and VIF. As described in Sec. III-D, both SSIM and PSNR are common metrics to evaluate DNNs for LDCT denoising. We include VIF, since it has been shown to have higher correlation with human readers for medical images [45], [46].

Conducting human reader studies is time-consuming and expensive and would render the application of the proposed benchmark setup to future algorithms impossible. To nevertheless evaluate the algorithms in terms of clinically relevant image properties, we include an analysis of radiomic features. To this end, we compare the similarity of radiomic features extracted on the denoised images to those extracted on the high-dose image.

Definition 1 (Radiomic feature similarity). *Let $\cos(x, y)$ be the cosine similarity between two vectors x and y :*

$$\cos(x, y) = \frac{x \cdot y}{\|x\| \|y\|}. \quad (4)$$

Further, let $A = \{0, 1, 2, \dots, n\}$, with n being the number of algorithms considered, and index 0 being associated with the high-dose image. We denote with $R_{i,j}^{(s)}$ the radiomic feature $j \in \{1, 2, \dots, J\}$ extracted on scan s associated with algorithm $i \in A$. In order to get a task-agnostic metric, we assign an equal a-priori importance to each feature by normalizing

$$\tilde{R}_{i,j}^{(s)} = \frac{R_{i,j}^{(s)} - \max_{k \in A} R_{k,j}^{(s)}}{\max_{k \in A} R_{k,j}^{(s)} - \min_{k \in A} R_{k,j}^{(s)}}. \quad (5)$$

The radiomic feature similarity $RFS_i^{(s)}$ of algorithm $i = 1, \dots, n$ on some scan s is then given as

$$RFS_i^{(s)} = \cos(r_i^{(s)}, r_0^{(s)}), \quad r_i^{(s)} = (\tilde{R}_{i,1}^{(s)}, \dots, \tilde{R}_{i,J}^{(s)}) . \quad (6)$$

Radiomic features are commonly extracted on segmentations of tumors or entire organs. On the high-dose scans of the test data, we therefore segment the following organs using the

¹We here omit evaluation of RMSE since it is related to the PSNR via $\text{PSNR} = 20 \log_{10} (I_{\text{max}}/\text{RMSE})$, with I_{max} being the maximum pixel value.

TABLE II

SUMMARY OF RESULTS ON THE METRICS SSIM, PSNR, AND VIF. WE HIGHLIGHTED A METRIC BOLD, IF IT IS SIGNIFICANTLY BETTER THAN THE PREVIOUSLY BEST METHOD ON THAT ANATOMY. LIKewise, WE HIGHLIGHTED A METRIC ITALICS, IF IT IS SIGNIFICANTLY WORSE THAN THE PREVIOUSLY BEST METHOD ON THAT ANATOMY.

	Chest (10% dose)			Abdomen (25% dose)			Head (25% dose)		
	SSIM	PSNR (dB)	VIF	SSIM	PSNR (dB)	VIF	SSIM	PSNR (dB)	VIF
LD	0.34	18.77	0.09	0.84	28.67	0.34	0.88	26.4	0.55
CNN-10 (2017)	0.5867 ± 0.0006	27.71 ± 0.02	0.1915 ± 0.0008	0.896 ± 0.001	32.4 ± 0.1	0.449 ± 0.003	0.896 ± 0.004	28.9 ± 0.6	0.620 ± 0.006
RED-CNN (2017)	0.609 ± 0.002	28.36 ± 0.03	0.221 ± 0.003	0.9028 ± 0.0007	33.22 ± 0.07	0.491 ± 0.008	0.904 ± 0.001	30.4 ± 0.2	0.69 ± 0.01
WGAN-VGG (2017)	<i>0.51 ± 0.03</i>	<i>25.5 ± 0.2</i>	<i>0.148 ± 0.004</i>	<i>0.882 ± 0.002</i>	<i>30.5 ± 0.9</i>	<i>0.38 ± 0.01</i>	<i>0.88 ± 0.02</i>	<i>25 ± 3</i>	<i>0.53 ± 0.02</i>
ResNet (2018)	0.610 ± 0.001	28.42 ± 0.03	0.224 ± 0.002	<i>0.901 ± 0.002</i>	<i>33.15 ± 0.08</i>	<i>0.487 ± 0.006</i>	<i>0.901 ± 0.005</i>	<i>29.6 ± 0.8</i>	<i>0.67 ± 0.02</i>
QAE (2019)	<i>0.584 ± 0.003</i>	<i>27.62 ± 0.09</i>	<i>0.186 ± 0.003</i>	<i>0.894 ± 0.002</i>	<i>32.0 ± 0.2</i>	<i>0.418 ± 0.007</i>	<i>0.899 ± 0.001</i>	<i>28.5 ± 0.3</i>	<i>0.594 ± 0.008</i>
DU-GAN (2021)	<i>0.565 ± 0.004</i>	<i>26.7 ± 0.1</i>	<i>0.168 ± 0.002</i>	<i>0.894 ± 0.002</i>	<i>32.1 ± 0.3</i>	<i>0.427 ± 0.005</i>	<i>0.903 ± 0.003</i>	<i>29 ± 1</i>	<i>0.622 ± 0.005</i>
TransCT (2021)	<i>0.563 ± 0.002</i>	<i>26.99 ± 0.05</i>	<i>0.167 ± 0.002</i>	<i>0.877 ± 0.003</i>	<i>30.5 ± 0.2</i>	<i>0.372 ± 0.007</i>	<i>0.849 ± 0.005</i>	<i>24.7 ± 0.4</i>	<i>0.44 ± 0.01</i>
Bilateral (2022)	<i>0.555 ± 0.001</i>	<i>25.59 ± 0.04</i>	<i>0.159 ± 0.002</i>	<i>0.859 ± 0.003</i>	<i>27.1 ± 0.1</i>	<i>0.361 ± 0.003</i>	<i>0.873 ± 0.002</i>	<i>26.6 ± 0.1</i>	<i>0.500 ± 0.004</i>

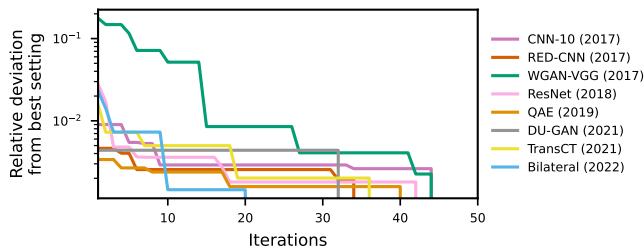


Fig. 2. Evolution of relative deviation from best setting over the 50 iterations of bayesian hyperparameter optimization. For each iteration i we show the relative deviation of the best network up to i from the final best configuration of hyperparameters (over all 50 iterations).

TotalSegmentator [63]: lung on chest scans, liver on abdomen scans, and brain on head scans. This segmentation mask is then used for subsequent extraction of 91 radiomic features² using PyRadiomics [64].

E. LDCT-hard benchmark dataset

In our experiments we find that the performance of all algorithms varies greatly, both between different exam types and images of the same exam type. The latter observation motivates us to derive a novel collection of test datasets, each of which being a subset of the *Low dose CT and Projection Dataset* [39]. We refer to LDCT-hard- $q\%$, as the subset containing the $q\%$ slices with lowest average SSIM across all evaluated methods. To not underrepresent anatomies for which methods achieve generally higher SSIMs (e.g., head), this subset is collected for each exam type separately.

V. RESULTS

A. Hyperparameter optimization

We first verify that all methods converged within the 50 iterations of Bayesian hyperparameter optimization (Fig. 2). To this end, we evaluate for each method and iteration i the relative deviation RelDev_i from the best setting w.r.t. the SSIM on the validation set

$$\text{RelDev}_i = 1 - \frac{\max_{j \leq i} \text{SSIM}_j}{\max_j \text{SSIM}_j}. \quad (7)$$

²This includes features from the following classes (# of features): first order statistics (18), gray level co-occurrence matrix (24), gray level run length matrix (16), gray level size zone matrix (16), neighbouring gray tone difference matrix (4), and gray level dependence matrix (13).

TABLE III

RADIOMIC FEATURE SIMILARITY FOR THREE ORGAN SEGMENTATIONS. BOLD NUMBERS INDICATE THAT A METHOD IS SIGNIFICANTLY BETTER THAN THE PREVIOUSLY BEST METHOD ON THAT ANATOMY. LIKewise, ITALICS INDICATE THAT IT IS SIGNIFICANTLY WORSE.

	Lung	Liver	Brain
LD	0.7	0.75	0.71
CNN-10 (2017)	0.800 ± 0.009	0.88 ± 0.02	0.94 ± 0.02
RED-CNN (2017)	<i>0.76 ± 0.02</i>	<i>0.80 ± 0.04</i>	<i>0.95 ± 0.02</i>
WGAN-VGG (2017)	0.98 ± 0.01	0.92 ± 0.05	<i>0.86 ± 0.07</i>
ResNet (2018)	<i>0.75 ± 0.02</i>	<i>0.79 ± 0.06</i>	<i>0.91 ± 0.05</i>
QAE (2019)	<i>0.83 ± 0.02</i>	0.96 ± 0.01	<i>0.95 ± 0.02</i>
DU-GAN (2021)	<i>0.965 ± 0.007</i>	0.967 ± 0.008	<i>0.94 ± 0.08</i>
TransCT (2021)	<i>0.83 ± 0.01</i>	<i>0.92 ± 0.01</i>	<i>0.88 ± 0.04</i>
Bilateral (2022)	<i>0.64 ± 0.01</i>	<i>0.87 ± 0.02</i>	<i>0.873 ± 0.006</i>

We find that hyperparameter optimization for most of the methods converged within the first 40 iterations and none of the methods improved in the last five iterations (c.f. intercept with x-axis in Fig. 2). For all methods $\text{RelDev}_{i \geq 30} < 0.5\%$.

B. Evaluation using standard image quality metrics

We then evaluate all algorithms using the following image quality metrics: SSIM, PSNR, and VIF (Tab. II). For each method, we test if it performs significantly better or worse than the previously best method, using the nonparametric *Mann-Whitney U* test [65] with significance level $\alpha = 5\%$. While we find that ResNet significantly outperforms previous methods on the chest data, none of the newer methods consistently outperforms RED-CNN, one of the earliest deep-learning based methods for LDCT denoising (c.f. **bold** numbers in Tab. II). On the contrary, for many configurations newer methods perform significantly worse than RED-CNN (c.f. *italic* numbers in Tab. II). In particular, we find that the two newest methods considered in this study (TransCT and Bilateral) perform significantly worse w.r.t. all metrics and exam types compared to RED-CNN. Remarkably, they even perform significantly worse compared to the low-dose scan on few metric and exam type combinations (e.g., TransCT on head scans for all metrics; Bilateral on abdomen scans for PSNR).

C. Evaluation using radiomic feature similarity

We further evaluate all algorithms using the radiomic feature similarity in order to better assess whether the differences observed in the previous section translate to clinical features.

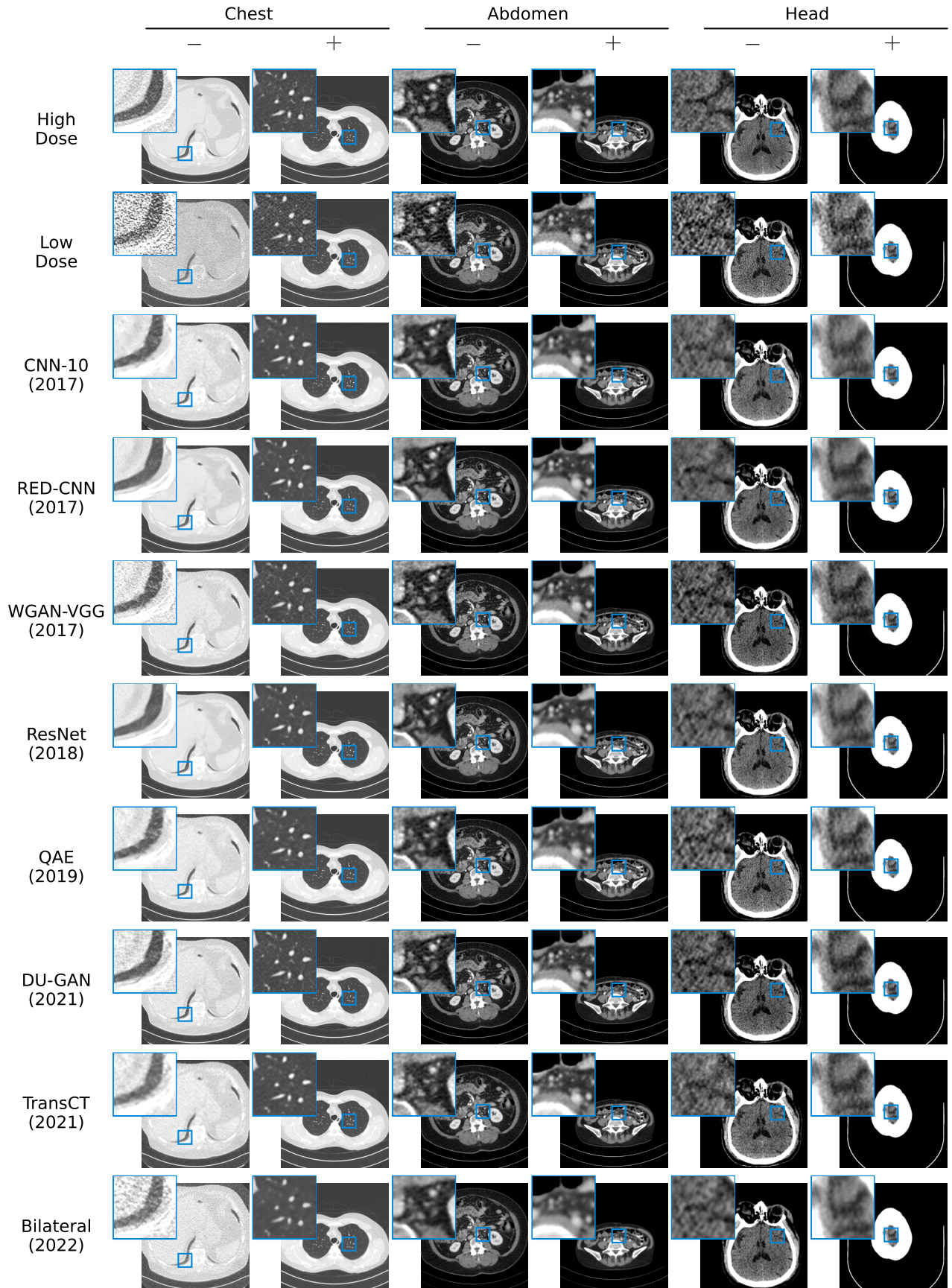


Fig. 3. Best viewed zoomed in. Slices from the test dataset, for which the average SSIM over all methods is lowest (-) and highest (+). For each method, we show results for the best performing network (over the ten random trials), *i.e.*, network having the highest SSIM on the validation data.

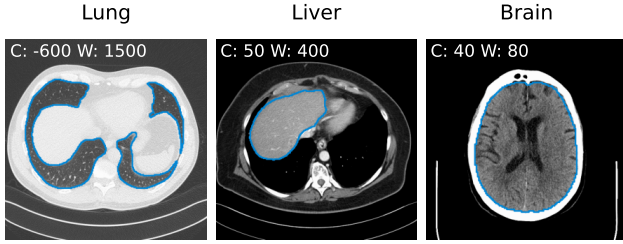


Fig. 4. Contour plots of automatic segmentations for three high-dose scans of the test set of lung, liver, and brain. Radiomic features were extracted within these segmentations for low- and high-dose as well as all denoised volumes.

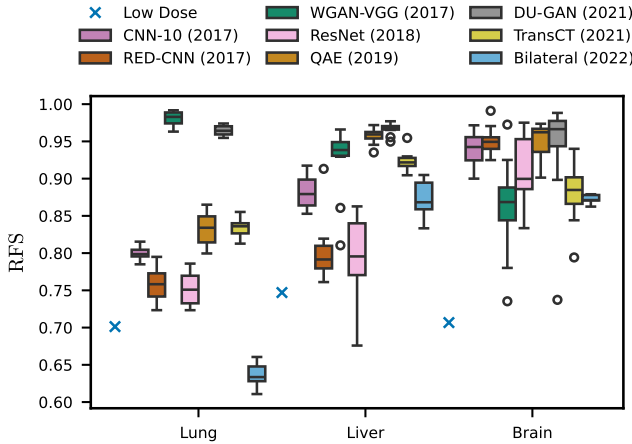


Fig. 5. Radiomic feature similarity for different exam types and methods. Individual samples correspond to mean RFS over all scans of an anatomy for a single trained network. Box plots were then drawn over the ten training runs with different random seeds (c.f. Sec. IV-C).

In Fig. 4 we show contour plots of the automatic segmentations of the brain, lung, and liver for three high-dose scans of the test set. We visually verify that segmentations are reasonably good for all 15 scans in the test set. Those segmentation masks are then used to extract radiomic features for all low- and high-dose, as well as all denoised volumes of the test set. Using the same segmentation mask for subsequent radiomic feature extraction of all algorithms ensures a fair comparison, despite possible small errors produced by the automatic segmentation pipeline.

Upon evaluation of the radiomic feature similarity (Tab. III & Fig. 5), we find that radiomic features extracted for all denoising methods are significantly more similar to those extracted on the high-dose scan, compared to features extracted on the low dose scan, with Bilateral on lung data being the only exception. We also find that contrary to our findings using standard image quality metrics, RED-CNN is outperformed by numerous other algorithms, including the (older) CNN-10, and newer algorithms such as WGAN-VGG and QAE. Remarkably, the two GAN-based algorithms WGAN-VGG and DUGAN outperform all other algorithms on the lung data by a large margin. We hypothesize that this is due to the lower dose (10% vs. 25% for all other anatomies) on that data and the ability of GANs to produce more realistic noise textures in high-ambiguity settings compared to methods trained with

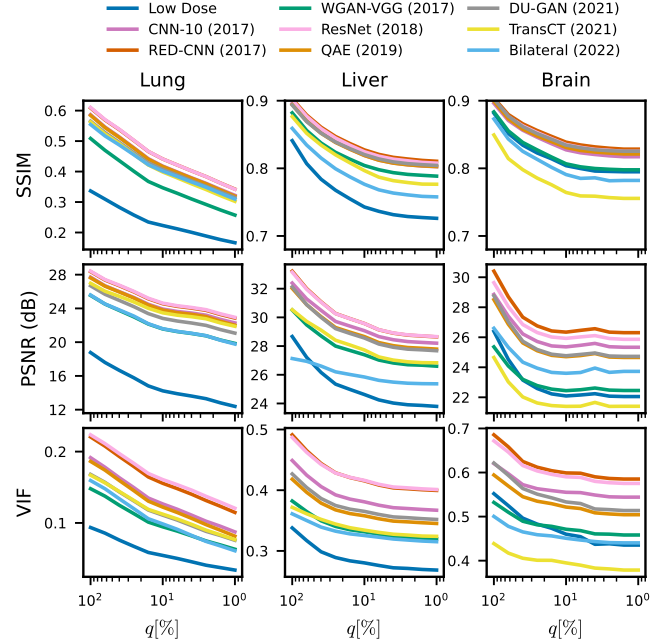


Fig. 6. Evaluation of all methods for LDCT-hard-q% for different values of q (right is smaller). For some settings and anatomies, methods perform up to 50% worse for small q . The regular test set corresponds to $q=100\%$. Error bars were omitted to improve visibility.

standard pixelwise loss functions [66]. Nonetheless, we do not find newer algorithms to consistently outperform older ones, and particularly the two newest algorithms considered in our study (TransCT and Bilateral) perform significantly worse w.r.t. radiomic feature similarity of all organs compared to older methods.

D. Evaluation on LDCT-hard datasets

Figure 6 shows the performance of individual methods for increasingly hard subsets of the training data (i.e., smaller q). We find a strong correlation between metrics for each method and the low dose scan. Although not surprising, this indicates that methods perform increasingly worse for increasing deviations of the low dose scan from the high dose scan. Additionally, the ranking among methods remains mostly invariant to q , and thus we conclude that all methods are similar in terms of their robustness to different amounts of deterioration of the low dose scan. Remarkably, WGAN-VGG, having a lower VIF and PSNR compared to the low dose scan on head exams for the regular test set (corresponding to $q = 100\%$), has a higher VIF and PSNR compared to the low dose scan for more difficult slices ($q \geq 16\%$ for VIF, $q \geq 40\%$ for PSNR). This may be explained by the aforementioned ability of GANs to produce more realistic results in high-ambiguity settings compared to networks trained in a pixelwise fashion.

Figure 3 shows qualitative results for the slices from the test dataset for which the average SSIM over all methods is lowest (-) and highest (+), respectively. As can be seen, for each anatomy, the slice maximizing the average SSIM is the one where the cross sectional area of the patient is small, thus reducing the noise in the low dose image.

VI. DISCUSSION

In this study, we revisited some of the numerous proposed deep learning-based algorithms for low dose CT image denoising. We discovered several limitations in the experimental setups of these methods that hinder the verifiability of their claimed improvements. To overcome these challenges, we proposed a novel benchmark setup that promotes fair and reproducible evaluations. The setup comprises a unified data preprocessing, rigorous hyperparameter optimization, and evaluation using various metrics, including a novel metric that measures the similarity of radiomic features between the denoised volume and the high dose scan.

Upon evaluation of eight deep-learning based denoising algorithms proposed over the past six years, we find that there has been little progress. Particularly, when evaluated using standard image quality measures such as SSIM and PSNR, we find that no method consistently outperforms one of the earliest methods, RED-CNN. When evaluated using the radiomic feature similarity, we find that algorithms trained with an adversarial loss significantly outperform methods trained with pixel-wise losses on some data, indicating that the radiomic feature similarity provides useful information beyond standard, nonclinical image quality metrics. Nonetheless, the newest algorithms considered in our study fail to consistently outperform older ones. We also evaluated all methods on subsets of the test data consisting of increasingly difficult slices and find that methods are similarly robust to different amounts of deterioration of the low dose scan.

Similar to ‘reality checks’ in related fields [67], [68], our study highlights the need for a more rigorous and fair evaluation of novel deep learning-based denoising methods for low dose CT image denoising. We believe that our benchmark setup is a first and important step towards this direction and will help to develop novel and better algorithms.

REFERENCES

- [1] M. K. Kalra, M. M. Maher, T. L. Toth, L. M. Hamberg, M. A. Blake, J.-A. Shepard, and S. Saini, “Strategies for CT radiation dose optimization,” *Radiology*, vol. 230, no. 3, pp. 619–628, Mar. 2004.
- [2] D. J. Brenner and E. J. Hall, “Computed tomography—an increasing source of radiation exposure,” *The New England Journal of Medicine*, vol. 357, no. 22, pp. 2277–2284, Nov. 2007.
- [3] A. Ziegler, T. Koehler, and R. Proksa, “Noise and resolution in images reconstructed with FBP and OSC algorithms for CT,” *Med. Phys.*, vol. 34, no. 2, pp. 585–598, 2007.
- [4] E. Y. Sidky, C. Kao, and X. Pan, “Accurate image reconstruction from few-views and limited-angle data in divergent-beam CT,” *Journal of X-Ray Science and Technology*, vol. 14, pp. 119–139, 2006.
- [5] M. Balda, J. Hornegger, and B. Heismann, “Ray contribution masks for structure adaptive sinogram filtering,” *IEEE Transactions on Medical Imaging*, vol. 31, no. 6, pp. 1228–1239, Jun. 2012.
- [6] P. F. Feruglio, C. Vinegoni, J. Gros, A. Sbarbati, and R. Weissleder, “Block matching 3D random noise filtering for absorption optical projection tomography,” *Physics in medicine and biology*, vol. 55, no. 18, pp. 5401–5415, Sep. 2010.
- [7] Z. Li, L. Yu, J. D. Trzasko, D. S. Lake, D. J. Blezek, J. G. Fletcher, C. H. McCollough, and A. Manduca, “Adaptive nonlocal means filtering based on local noise level for CT denoising,” *Medical Physics*, vol. 41, no. 1, p. 011908, 2014.
- [8] A. Manduca, L. Yu, J. D. Trzasko, N. Khaylova, J. M. Koffler, C. M. McCollough, and J. G. Fletcher, “Projection space denoising with bilateral filtering and CT noise modeling for dose reduction in CT,” *Medical Physics*, vol. 36, no. 11, pp. 4911–4919, 2009.
- [9] P. Sukovic and N. Clinthorne, “Penalized weighted least-squares image reconstruction for dual energy X-ray transmission tomography,” *IEEE Transactions on Medical Imaging*, vol. 19, no. 11, pp. 1075–1081, Nov. 2000.
- [10] H. Chen, Y. Zhang, W. Zhang, P. Liao, K. Li, J. Zhou, and G. Wang, “Low-dose CT denoising with convolutional neural network,” in *2017 IEEE 14th International Symposium on Biomedical Imaging (ISBI 2017)*, Apr. 2017, pp. 143–146.
- [11] —, “Low-dose CT via convolutional neural network,” *Biomedical Optics Express*, vol. 8, no. 2, pp. 679–694, Jan. 2017.
- [12] H. Chen, Y. Zhang, M. K. Kalra, F. Lin, Y. Chen, P. Liao, J. Zhou, and G. Wang, “Low-dose CT with a residual encoder-decoder convolutional neural network,” *IEEE Transactions on Medical Imaging*, vol. 36, no. 12, pp. 2524–2535, Dec. 2017.
- [13] F. Fan, H. Shan, M. K. Kalra, R. Singh, G. Qian, M. Getzin, Y. Teng, J. Hahn, and G. Wang, “Quadratic autoencoder (Q-AE) for low-dose CT denoising,” *IEEE Transactions on Medical Imaging*, vol. 39, no. 6, pp. 2035–2050, Jun. 2020.
- [14] M. P. Heinrich, M. Stille, and T. M. Buzug, “Residual U-Net convolutional neural network architecture for low-dose CT denoising,” *Current Directions in Biomedical Engineering*, vol. 4, no. 1, pp. 297–300, Sep. 2018.
- [15] Z. Huang, J. Zhang, Y. Zhang, and H. Shan, “DU-GAN: Generative adversarial networks with dual-domain U-Net-based discriminators for low-dose CT denoising,” *IEEE Transactions on Instrumentation and Measurement*, vol. 71, pp. 1–12, 2022.
- [16] E. Kang, J. Min, and J. C. Ye, “A deep convolutional neural network using directional wavelets for low-dose X-ray CT reconstruction,” *Medical Physics*, vol. 44, no. 10, pp. e360–e375, 2017.
- [17] S. Ramanathan and M. Ramasundaram, “Low dose CT image reconstruction using deep convolutional residual learning network,” *SN Computer Science*, vol. 4, no. 6, p. 720, Sep. 2023.
- [18] H. Shan, A. Padole, F. Homayounieh, U. Kruger, R. D. Khera, C. Nitwarangkul, M. K. Kalra, and G. Wang, “Competitive performance of a modularized deep neural network compared to commercial algorithms for low-dose CT image reconstruction,” *Nature Machine Intelligence*, vol. 1, no. 6, pp. 269–276, Jun. 2019.
- [19] F. Wagner, M. Thies, M. Gu, Y. Huang, S. Pechmann, M. Patwari, S. Ploner, O. Aust, S. Uderhardt, G. Schett, S. Christiansen, and A. Maier, “Ultralow-parameter denoising: Trainable bilateral filter layers in computed tomography,” *Medical Physics*, vol. 49, no. 8, pp. 5107–5120, 2022.
- [20] Q. Yang, P. Yan, Y. Zhang, H. Yu, Y. Shi, X. Mou, M. K. Kalra, Y. Zhang, L. Sun, and G. Wang, “Low-dose CT image denoising using a generative adversarial network with wasserstein distance and perceptual loss,” *IEEE Transactions on Medical Imaging*, vol. 37, no. 6, pp. 1348–1357, Jun. 2018.
- [21] S. Yang, Q. Pu, C. Lei, Q. Zhang, S. Jeon, and X. Yang, “Low-dose CT denoising with a high-level feature refinement and dynamic convolution network,” *Medical Physics*, vol. 50, no. 6, pp. 3597–3611, 2023.
- [22] Z. Zhang, L. Yu, X. Liang, W. Zhao, and L. Xing, “TransCT: Dual-path transformer for low dose computed tomography,” in *MICCAI*, 2021.
- [23] T. Humphries, S. Coulter, D. Si, M. Simms, and R. King, “Comparison of deep learning approaches to low dose CT using low intensity and sparse view data,” in *Medical Imaging 2019: Physics of Medical Imaging*, H. Bosmans, G.-H. Chen, and T. Gilat Schmidt, Eds. San Diego, United States: SPIE, Mar. 2019, p. 156.
- [24] Y.-J. Ma, Y. Ren, P. Feng, P. He, X.-D. Guo, and B. Wei, “Sinogram denoising via attention residual dense convolutional neural network for low-dose computed tomography,” *Nuclear Science and Techniques*, vol. 32, no. 4, p. 41, Apr. 2021.
- [25] L. Yang, Z. Li, R. Ge, J. Zhao, H. Si, and D. Zhang, “Low-dose CT denoising via sinogram inner-structure transformer,” *IEEE Transactions on Medical Imaging*, vol. 42, no. 4, pp. 910–921, Apr. 2023.
- [26] E. Zainulina, A. Chernyavskiy, and D. V. Dylow, “No-reference denoising of low-dose CT projections,” in *2021 IEEE 18th International Symposium on Biomedical Imaging (ISBI)*, Apr. 2021, pp. 77–81.
- [27] Z. Hong, D. Zeng, X. Tao, and J. Ma, “Learning CT projection denoising from adjacent views,” *Medical Physics*, vol. 50, no. 3, pp. 1367–1377, 2023.
- [28] A. M. Cormack, “Representation of a function by Its line integrals, with some radiological applications,” *Journal of Applied Physics*, vol. 34, no. 9, pp. 2722–2727, 1963.
- [29] R. Gordon, R. Bender, and G. T. Herman, “Algebraic Reconstruction Techniques (ART) for three-dimensional electron microscopy and X-ray photography,” *Journal of Theoretical Biology*, vol. 29, no. 3, pp. 471–481, Dec. 1970.

- [30] A. H. Andersen and A. C. Kak, "Simultaneous Algebraic Reconstruction Technique (SART): A superior implementation of the ART algorithm," *Ultrasonic Imaging*, vol. 6, no. 1, pp. 81–94, Jan. 1984.
- [31] A. D. Missert, S. Leng, L. Yu, and C. H. McCollough, "Noise subtraction for low-dose CT images using a deep convolutional neural network," in *Proceedings of the Fifth International Conference on Image Formation in X-Ray Computed Tomography*, Salt Lake City, UT, USA, May 2018, pp. 399–402.
- [32] D. O. Bague, J. Leuschner, and M. Schmidt, "Computed tomography reconstruction using deep image prior and learned reconstruction methods," *Inverse Problems*, vol. 36, no. 9, p. 094004, Sep. 2020.
- [33] X. Yin, Q. Zhao, J. Liu, W. Yang, J. Yang, G. Quan, Y. Chen, H. Shu, L. Luo, and J.-L. Coatrieux, "Domain progressive 3D residual convolution network to improve low-dose CT imaging," *IEEE Transactions on Medical Imaging*, vol. 38, no. 12, pp. 2903–2913, Dec. 2019.
- [34] L. Chao, P. Zhang, Y. Wang, Z. Wang, W. Xu, and Q. Li, "Dual-domain attention-guided convolutional neural network for low-dose cone-beam computed tomography reconstruction," *Knowledge-Based Systems*, vol. 251, p. 109295, Sep. 2022.
- [35] Y. Zhang, D. Hu, Q. Zhao, G. Quan, J. Liu, Q. Liu, Y. Zhang, G. Coatrieux, Y. Chen, and H. Yu, "CLEAR: Comprehensive learning enabled adversarial reconstruction for subtle structure enhanced low-dose CT imaging," *IEEE Transactions on Medical Imaging*, vol. 40, no. 11, pp. 3089–3101, Nov. 2021.
- [36] B. Zhou, S. K. Zhou, J. S. Duncan, and C. Liu, "Limited view tomographic reconstruction using a cascaded residual dense spatial-channel attention network with projection data fidelity layer," *IEEE Transactions on Medical Imaging*, vol. 40, no. 7, pp. 1792–1804, Jul. 2021.
- [37] B. Zhou, X. Chen, H. Xie, S. K. Zhou, J. S. Duncan, and C. Liu, "Du-DoUFNet: Dual-domain under-to-fully-complete progressive restoration network for simultaneous metal artifact reduction and low-dose CT reconstruction," *IEEE Transactions on Medical Imaging*, vol. 41, no. 12, pp. 3587–3599, Dec. 2022.
- [38] C. H. McCollough, A. C. Bartley, R. E. Carter, B. Chen, T. A. Drees, P. Edwards, D. R. Holmes III, A. E. Huang, F. Khan, S. Leng, K. L. McMillan, G. J. Michalak, K. M. Nunez, L. Yu, and J. G. Fletcher, "Low-dose CT for the detection and classification of metastatic liver lesions: Results of the 2016 Low Dose CT Grand Challenge," *Medical Physics*, vol. 44, no. 10, pp. e339–e352, 2017.
- [39] C. McCollough, B. Chen, D. R. Holmes III, X. Duan, Z. Yu, L. Yu, S. Leng, and J. Fletcher, "Low dose CT image and projection data," 2020.
- [40] S. E. Divel and N. J. Pelc, "Accurate image domain noise insertion in CT images," *IEEE Transactions on Medical Imaging*, vol. 39, no. 6, pp. 1906–1916, Jun. 2020.
- [41] I. Horenko, L. Pospíšil, E. Vecchi, S. Albrecht, A. Gerber, B. Rehbock, A. Stroh, and S. Gerber, "Low-cost probabilistic 3D denoising with applications for ultra-low-radiation computed tomography," *Journal of Imaging*, vol. 8, no. 6, p. 156, Jun. 2022.
- [42] Z. Wang, A. Bovik, H. Sheikh, and E. Simoncelli, "Image quality assessment: From error visibility to structural similarity," *IEEE Transactions on Image Processing*, vol. 13, no. 4, pp. 600–612, Apr. 2004.
- [43] F. R. Verdun, D. Racine, J. G. Ott, M. J. Tapiovaara, P. Toroi, F. O. Bochud, W. J. H. Veldkamp, A. Schegerer, R. W. Bouwman, I. H. Giron, N. W. Marshall, and S. Edyvean, "Image quality in CT: From physical measurements to model observers," *Physica Medica*, vol. 31, no. 8, pp. 823–843, Dec. 2015.
- [44] G. P. Renieblas, A. T. Nogués, A. M. G. M.d, N. G. León, and E. G. del Castillo, "Structural similarity index family for image quality assessment in radiological images," *Journal of Medical Imaging*, vol. 4, no. 3, p. 035501, Jul. 2017.
- [45] K. Ohashi, Y. Nagatani, M. Yoshigoe, K. Iwai, K. Tsuchiya, A. Hino, Y. Kida, A. Yamazaki, and T. Ishida, "Applicability evaluation of full-reference image quality assessment methods for computed tomography images," *Journal of Imaging Informatics in Medicine*, vol. 36, no. 6, pp. 2623–2634, Dec. 2023.
- [46] A. Mason, J. Rioux, S. E. Clarke, A. Costa, M. Schmidt, V. Keough, T. Huynh, and S. Beyea, "Comparison of objective image quality metrics to expert radiologists' scoring of diagnostic quality of MR images," *IEEE Transactions on Medical Imaging*, vol. 39, no. 4, pp. 1064–1072, Apr. 2020.
- [47] H. Sheikh and A. Bovik, "Image information and visual quality," *IEEE Transactions on Image Processing*, vol. 15, no. 2, pp. 430–444, Feb. 2006.
- [48] S. Pan, J. Flores, C. T. Lin, J. W. Stayman, and G. J. Gang, "Generative adversarial networks and radiomics supervision for lung lesion synthesis," *Proceedings of SPIE—the International Society for Optical Engineering*, vol. 11595, p. 115950O, Feb. 2021.
- [49] L. Wei and W. Hsu, "Efficient and accurate spatial-temporal denoising network for low-dose CT scans," in *Medical Imaging with Deep Learning*, Apr. 2021.
- [50] M. Patwari, R. Gutjahr, R. Marcus, Y. Thali, A. F. Calvarons, R. Raupach, and A. Maier, "Reducing the risk of hallucinations with interpretable deep learning models for low-dose CT denoising: Comparative performance analysis," *Physics in Medicine & Biology*, vol. 68, no. 19, p. 19LT01, Oct. 2023.
- [51] R. Franzen, "Kodak lossless true color image suite." 1999.
- [52] D. Martin, C. Fowlkes, D. Tal, and J. Malik, "A database of human segmented natural images and its application to evaluating segmentation algorithms and measuring ecological statistics," in *Proceedings Eighth IEEE International Conference on Computer Vision. ICCV 2001*, vol. 2, Jul. 2001, pp. 416–423 vol.2.
- [53] L. Zhang, X. Wu, A. Buades, and X. Li, "Color demosaicking by local directional interpolation and nonlocal adaptive thresholding," *Journal of Electronic Imaging*, vol. 20, no. 2, p. 023016, Apr. 2011.
- [54] J.-B. Huang, A. Singh, and N. Ahuja, "Single image super-resolution from transformed self-exemplars," in *2015 IEEE Conference on Computer Vision and Pattern Recognition (CVPR)*. Boston, MA, USA: IEEE, Jun. 2015, pp. 5197–5206.
- [55] K. Zhang, W. Zuo, Y. Chen, D. Meng, and L. Zhang, "Beyond a Gaussian denoiser: Residual learning of deep CNN for image denoising," *IEEE Transactions on Image Processing*, vol. 26, no. 7, pp. 3142–3155, Jul. 2017.
- [56] J. Bergstra, R. Bardenet, Y. Bengio, and B. Kégl, "Algorithms for hyper-parameter optimization," in *Advances in Neural Information Processing Systems*, vol. 24. Curran Associates, Inc., 2011.
- [57] J. Bergstra and Y. Bengio, "Random search for hyper-parameter optimization," *Journal of Machine Learning Research*, vol. 13, no. 10, pp. 281–305, 2012.
- [58] J. Snoek, H. Larochelle, and R. P. Adams, "Practical bayesian optimization of machine learning algorithms," in *Advances in Neural Information Processing Systems*, vol. 25. Curran Associates, Inc., 2012.
- [59] C. Liu, C. Gao, X. Xia, D. Lo, J. Grundy, and X. Yang, "On the reproducibility and replicability of deep learning in software engineering," *ACM Transactions on Software Engineering and Methodology*, vol. 31, no. 1, pp. 15:1–15:46, Oct. 2021.
- [60] I. Goodfellow, J. Pouget-Abadie, M. Mirza, B. Xu, D. Warde-Farley, S. Ozair, A. Courville, and Y. Bengio, "Generative Adversarial Nets," in *Advances in Neural Information Processing Systems*, vol. 27. Curran Associates, Inc., 2014.
- [61] M. Arjovsky, S. Chintala, and L. Bottou, "Wasserstein generative adversarial networks," in *Proceedings of the 34th International Conference on Machine Learning*. PMLR, Jul. 2017, pp. 214–223.
- [62] E. Schonfeld, B. Schiele, and A. Khoreva, "A U-Net based discriminator for generative adversarial networks," in *2020 IEEE/CVF Conference on Computer Vision and Pattern Recognition (CVPR)*. Seattle, WA, USA: IEEE, Jun. 2020, pp. 8204–8213.
- [63] J. Wasserthal, H.-C. Breit, M. T. Meyer, M. Pradella, D. Hinck, A. W. Sauter, T. Heye, D. T. Boll, J. Cyriac, S. Yang, M. Bach, and M. Segeroth, "TotalSegmentator: Robust segmentation of 104 anatomic structures in CT images," *Radiology: Artificial Intelligence*, vol. 5, no. 5, p. e230024, Sep. 2023.
- [64] J. J. M. van Griethuysen, A. Fedorov, C. Parmar, A. Hosny, N. Aucoin, V. Narayan, R. G. H. Beets-Tan, J.-C. Fillion-Robin, S. Pieper, and H. J. W. L. Aerts, "Computational radiomics system to decode the radiographic phenotype," *Cancer Research*, vol. 77, no. 21, pp. e104–e107, Nov. 2017.
- [65] H. B. Mann and D. R. Whitney, "On a test of whether one of two random variables is stochastically larger than the other," *The Annals of Mathematical Statistics*, vol. 18, no. 1, pp. 50–60, Mar. 1947.
- [66] H. Zhao, O. Gallo, I. Frosio, and J. Kautz, "Loss functions for image restoration with neural networks," *IEEE Transactions on Computational Imaging*, vol. 3, no. 1, pp. 47–57, Mar. 2017.
- [67] G. Melis, C. Dyer, and P. Blunsom, "On the state of the art of evaluation in neural language models," in *International Conference on Learning Representations*, Feb. 2018.
- [68] K. Musgrave, S. Belongie, and S.-N. Lim, "A metric learning reality check," in *Computer Vision – ECCV 2020*, ser. Lecture Notes in Computer Science, A. Vedaldi, H. Bischof, T. Brox, and J.-M. Frahm, Eds. Cham: Springer International Publishing, 2020, pp. 681–699.